SCIENCE CHINA
Earth Sciences

•ARTICLE•

September 2024 Vol.67 No.9: 2810–2823
https://doi.org/10.1007/s11430-023-1324-y

Relationship between seismic structures and the diverse rupture processes of the 2023 Türkiye earthquake doublet

Zhi WANG[1,2*], Yi FU[1,4] & Shunping PEI[3]

[1] *CAS Key Laboratory of Ocean and Marginal Sea Geology, South China Sea Institute of Oceanology, Chinese Academy of Sciences, Guangzhou 510301, China;*
[2] *Southern Marine Science and Engineering Guangdong Laboratory (Guangzhou), Guangzhou 511458, China;*
[3] *Key Laboratory of Tibetan Plateau Earth System, Environment and Resources (TPESER), Institute of Tibetan Plateau Research, Chinese Academy of Sciences, Beijing 100101, China;*
[4] *University of Chinese Academy of Sciences, Beijing 100049, China*

Received August 14, 2023; revised March 2, 2024; accepted April 15, 2024; published online August 8, 2024

Abstract Recent geodetic and seismological observations of two major earthquakes in southeastern Türkiye in February 2023 have revealed complex rupture initiation, propagation, and segmentation along the East Anatolian Fault Zone (EAFZ) and surrounding regions. However, the role of upper crust structures along the EAFZ in determining the diverse rupture processes of this earthquake doublet remains unclear. To further investigate this, we employed double-difference location and seismic tomography techniques to determine high-resolution seismic velocities (V_P, V_S) and Poisson's ratio (σ) structures using a multi-parameter joint tomographic algorithm. Our dataset includes 100,833 high-quality source-receiver travel-time pairs of P- and S-waves. We find that the unique rupture processes of this earthquake doublet were primarily influenced by contrasting crustal seismic structures and localized geological settings. The M_w7.8 mainshock was initiated within a transitional edge zone characterized by a rigid part (asperity) of the seismogenic zone with sharp contrast variations in rock strength ranging from low to high along the EAFZ. In comparison, the M_w7.6 rupture originated in a ductile belt featuring fluid saturation with low-V_P, low-V_S, and high-σ values that extended parallel to the Çardak Fault. The pronounced contrast structures observed along the former rupture can be attributed to the oblique collision system between the weakened section of the east Anatolian plateau and the brittle Arabian platform, while the latter rupture was initiated within the ductile structure associated with fluid intrusion caused by the northward subduction of the Cyprus slab and subsequent detachment. Furthermore, the occurrence of the first earthquake (E1) serves to alleviate shear stress on the second earthquake (E2) fault, potentially impeding the initiation of an E2 rupture. On the contrary, this event also significantly reduces the normal stress acting on the E2 fault due to a double left-lateral strike-slip system within a triangular region. This reduction not only results in a decrease of fault friction force and an increase in rock porosity but also induces lower strain drops and the redistribution of Coulomb stress, thereby contributing to the initiation of the E2 event. The proposed rupture pattern exceeds the conventional model that governs individual earthquake ruptures, offering new insights for mitigating potential seismic disasters in Türkiye. The lessons learned from this doublet event can contribute to reevaluating the ongoing risk of damaging earthquakes in China's South-North Seismic Zone or other regions worldwide with comparable geological conditions.

Keywords 2023 Türkiye earthquake doublet, Joint seismic tomography, Tomographic transition edge, Seismic rupture process, Strong fault coupling

Citation: Wang Z, Fu Y, Pei S. 2024. Relationship between seismic structures and the diverse rupture processes of the 2023 Türkiye earthquake doublet. Science China Earth Sciences, 67(9): 2810–2823, https://doi.org/10.1007/s11430-023-1324-y

---

* Corresponding author (email: zhiwang@scsio.ac.cn)

1. Introduction

Understanding the mechanism of earthquake nucleation and its complex rupture process is essential for forecasting the future occurrence of large damaging earthquakes and mitigating associated seismic hazards. Aiming at these scientific problems, many previous studies on a single earthquake were carried out and achieved a wealth of important results, but few to the earthquake doublet, which refers to two earthquakes that occurred closely in space and time and had similar magnitudes (Kagan and Jackson, 1999). Due to the lack of research objectives and seismic data for research, the external factors that control the timing, location, and other rupture properties of doublet are still unclear. On February 6th, 2023, two great crustal earthquakes occurred in eastern Türkiye's collision zone between the Arabian and Anatolian plates (Dal Zilio and Ampuero, 2023; Hall, 2023; Hussain et al., 2023). The first earthquake with M_w7.8 (moment magnitude) was initiated at the Sakçagöz-Narlı segment of the Dead Sea Fault (DSF) and then jumped onto the East Anatolian Fault (EAF) and ruptured bilaterally for more than 300 km (Melgar et al., 2023; Barbot et al., 2023; Ren et al., 2024; Meng et al., 2024). About 9 hours later, another M_w7.6 earthquake occurred near the Çardak Fault, a northwest branch fault of the EAFZ located about 100 km north of the first event (Figure 1a). The 2023 Türkiye earthquake doublet took place at the triple junction of Anatolia, Arabia, and Africa plates between the EAF and Çardak Fault, where a tectonic slip deficit of approximately 10 mm/yr accumulates along the fault zones (Figure 1a). GPS data reveals a northwestward movement of approximately 16 mm/yr for the Arabian plate and an anticlockwise rotation of 20 mm/yr for the Anatolian plateau (e.g., Gülerce et al., 2017; Turkelli et al., 2003). As a consequence, the east Anatolia and Çardak faults have predominately left-lateral strike-slip motions, giving rise to a distinctive triangular strike-slip system (Kahle et al., 2000; Medved et al., 2021) (Figure 1a).

Both events were widely felt and caused significant damages and casualties in southern and central Türkiye, and northwestern Syria as well (Figure 1a). While many studies have focused on the rupture processes of this doublet, the detailed seismological structures hosting both events are still unclear. In addition, it is still unclear how fault zone properties and regional velocity structures affect the timing and rupture properties of both mainshocks. To gain a deeper understanding of the factors contributing to the complexity of rupture processes, we determined high-resolution velocity structures and relocated earthquake catalogs in the aftershock zones of the 2023 doublet. We applied a joint seismic tomography approach that integrates both P and S seismic velocities (V_P, V_S) and V_P/V_S ratio to map Poisson's ratio (σ) using a large number of arrival times of P- and S-wave pairs (Figure 2b). Meanwhile, we utilized the double-difference (DD) location algorithm (Waldhauser and Ellsworth, 2000; Wang and Zhao, 2006) to improve the hypocenter accuracy of the aftershocks (Figure 3), which in turn could enhance the resolution of our seismic tomographic models. Finally, we analyzed the correlations among variations in the crustal seismic structure, strike-slip faults, and spatiotemporal distribution of aftershocks to elucidate the rupture processes of the 2023 Türkiye doublet.

2. Materials and method

2.1 Seismic data selection

In order to acquire high-resolution multi-parameter seismic structures of the crust, two sets of P- and S-wave arrival times from local events are collected for source-receiver pairs (Figure 2). The first set includes 3,812 events and 35,154 pairs of P- and S-wave arrivals spanning from January 3rd, 2014, to February 6th, 2023; whereas the second set comprises 65,679 P- and S-wave pairs obtained from 5,552 aftershocks of the earthquake doublet that occurred between February 6th to March 30th in the year (Table 1). The arrival-time data were obtained from the reviewed bulletin of the AFAD (Turkish Earthquake Data Center System Regulation, https://deprem.afad.gov.tr/event-catalog).

We applied multiple criteria to select two groups of arrival times: (1) Events with magnitudes greater than 1.0; (2) each event recorded at more than five pairs of data for the first group and over eight pairs for the second group within the study region; (3) Absolute values of raw travel-time residuals are less than 2.5 s for P phases and 3.0 s for S phases; (4) To ensure a uniform distribution of local events, we divided the study area into cubic blocks measuring 0.1°×0.1°× 1 km, selecting only one event from multiple events in each cubic block that has maximum numbers of P- and S-wave arrival times. Furthermore, based on the relationship between hypocenter distance and travel time, data points deviating from the fitted curve were excluded for each selected seismic phase (Figure 2a). The results of curve fitting for the first data group indicate that Pg and Sg travel times exhibit optimal data quality when epicentral distances are less than 120 km. In contrast, Pn and Sn travel times are predominantly observed within the 120–400 km range. Consequently, a multitude of seismic ray paths encompassing Pg, Sg, Pn, and Sn phases from both upper crustal and lower crustal earthquakes densely sample the entire region of interest's crust (Figure 2b). Ultimately, we selected a total of 100,833 source-receiver pairs for P- and S-wave arrival times derived from 9,364 local events recorded by 238 seismic stations to facilitate joint seismic tomography and hypocenter relocations (Table 1).

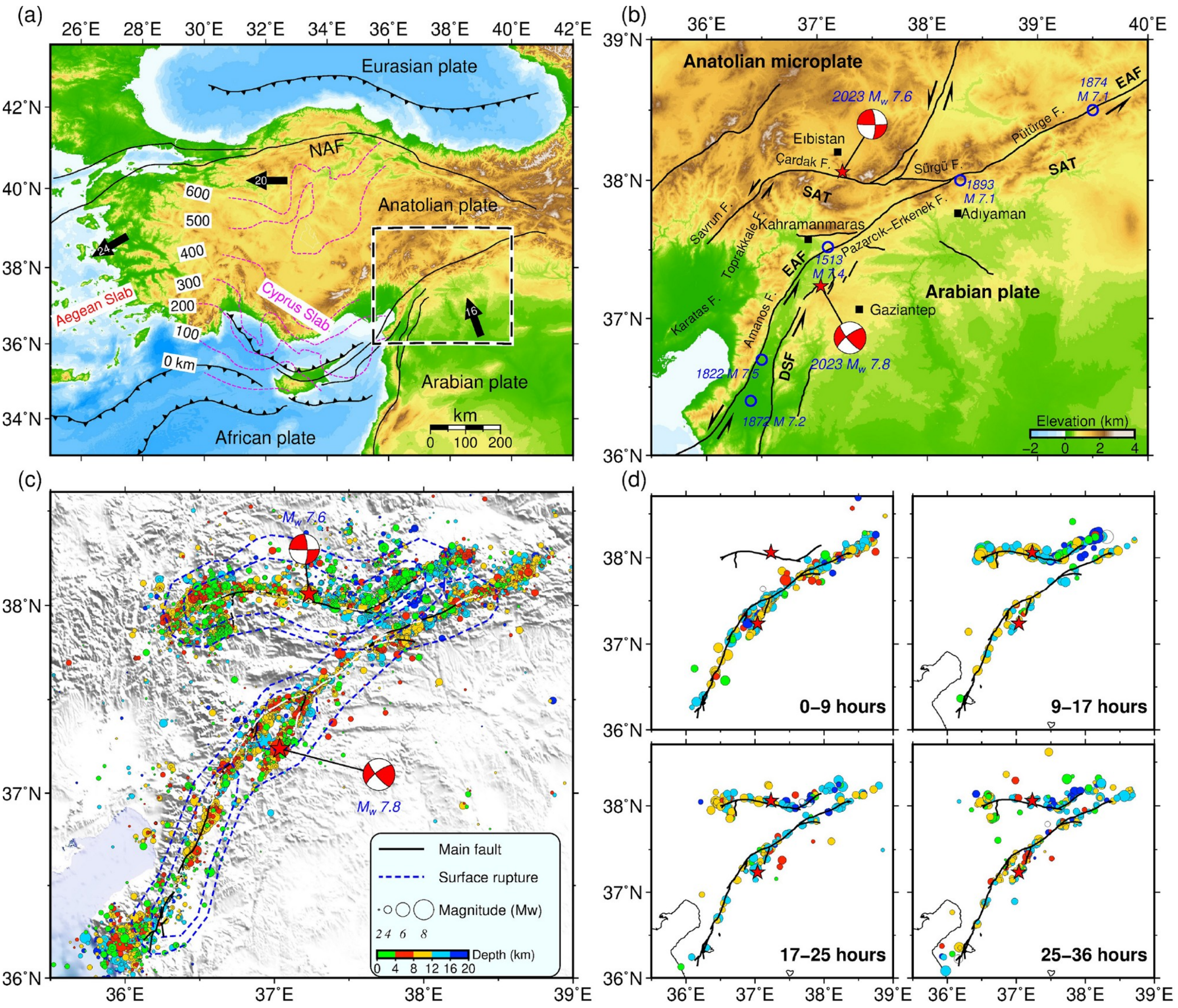

Figure 1 Maps showing regional tectonic settings, *M*7+ historical earthquakes, active faults, and aftershocks following the 2023 earthquake doublet. (a) The main plate boundaries and depth contours of slabs. The black sawtooth lines denote the direction of motions between different plates. Black lines depict plate boundaries, while pink dashed lines with numbers represent the depth contours of the Cyprean and Aegean slabs based on the seismic tomographic model of Kounoudis et al. (2020). NAF, North Anatolian Fault. A black dashed rectangle outlines the source region of the 2023 Türkiye earthquake doublet. (b) Tectonics, features, primary main rupture faults, and associated earthquakes. Two red stars represent the relocated epicenters of the M_w7.8 and 7.6 earthquakes. Black lines depict active faults (Emre et al., 2018), and blue circles denote large historical events with magnitudes greater than 7.0 (Duman and Emre, 2013). A gray sawtooth line signifies the location of the Southeast Anatolian Thrust (SAT) front. EAF, East Anatolian Fault; DSF, Dead Sea Fault; SAT, Southeast Anatolian thrust. (c) The distribution of aftershocks relocated using the double-difference method. Each circle represents one aftershock, with size proportional to the magnitude and color dependent on depth. Blue dashed lines indicate the surface rupture zones. (d) The spatiotemporal distribution of early aftershocks occurring within 36 hours since the first rupture.

2.2 Initialization of parameter

For seismic tomography and hypocenter relocation, a one-dimensional (1-D) initial velocity model is crucial in determining the final results (Figure 3a). We evaluated several previous 1-D models by assessing their consistency with arrival times (e.g., Kaviani et al., 2020; Medved et al., 2021; Pasyanos et al., 2014). Ultimately, we selected layered velocity values from a recent investigation (Medved et al., 2021) as our 1-D initial velocity model based on their ability to minimize the root-mean-square (RMS) of travel-time residues (Figure 4). Figure 3 depicts the 1-D initial model (a), the grid model (b) utilized for hypocenter location and tomographic inversion, and the trade-off between travel time residuals and model variations (c). The final 1-D model is a horizontal average of the inverted 3-D model. After examining their effects on the final checkerboard resolution tests, a grid model with a horizontal interval of 0.2° and vertical intervals ranging from 3 km to 10 km (Figure 3b) was adopted. The grid nodes with hit counts exceeding 10 are incorporated into the inversion process. An appropriate damping parameter of 25 is determined by referencing trade-

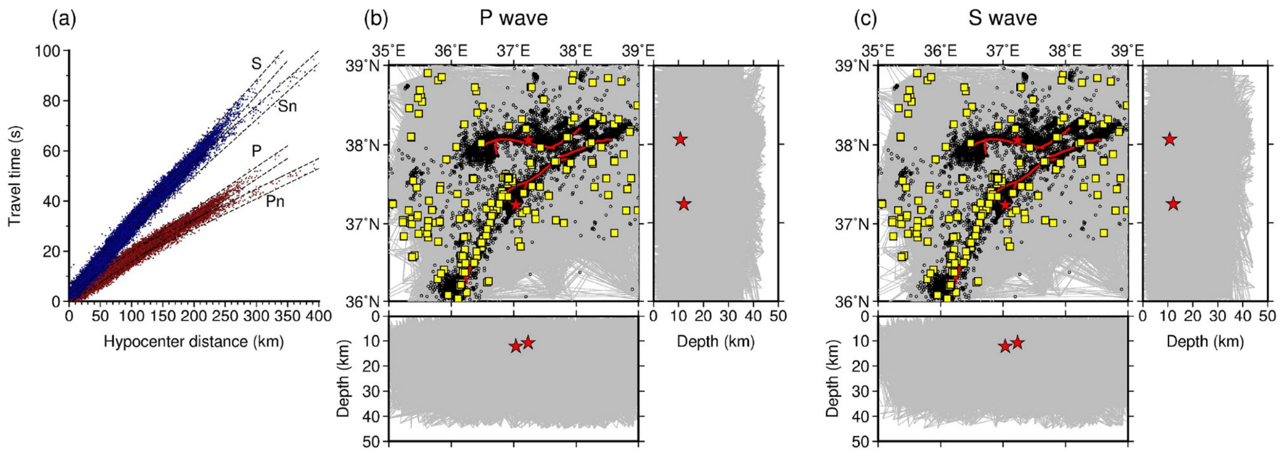

Figure 2 The distribution of P- and S-wave travel times, seismic stations, and earthquakes were utilized in this study. (a) A plot showing the distance from the epicenter plotted against travel times for both P- and S-phases. The dashed lines represent the travel-time residuals of ±2.5 s for P phases and ±3.0 s for S phases, respectively. (b) Depicted are the ray paths of P-waves along with seismic stations and events. (c) Similar to (b) but specifically for S-wave. The yellow squares indicate the stations used for inversion analysis. Two red stars denote the locations of the two mainshock hypocenters.

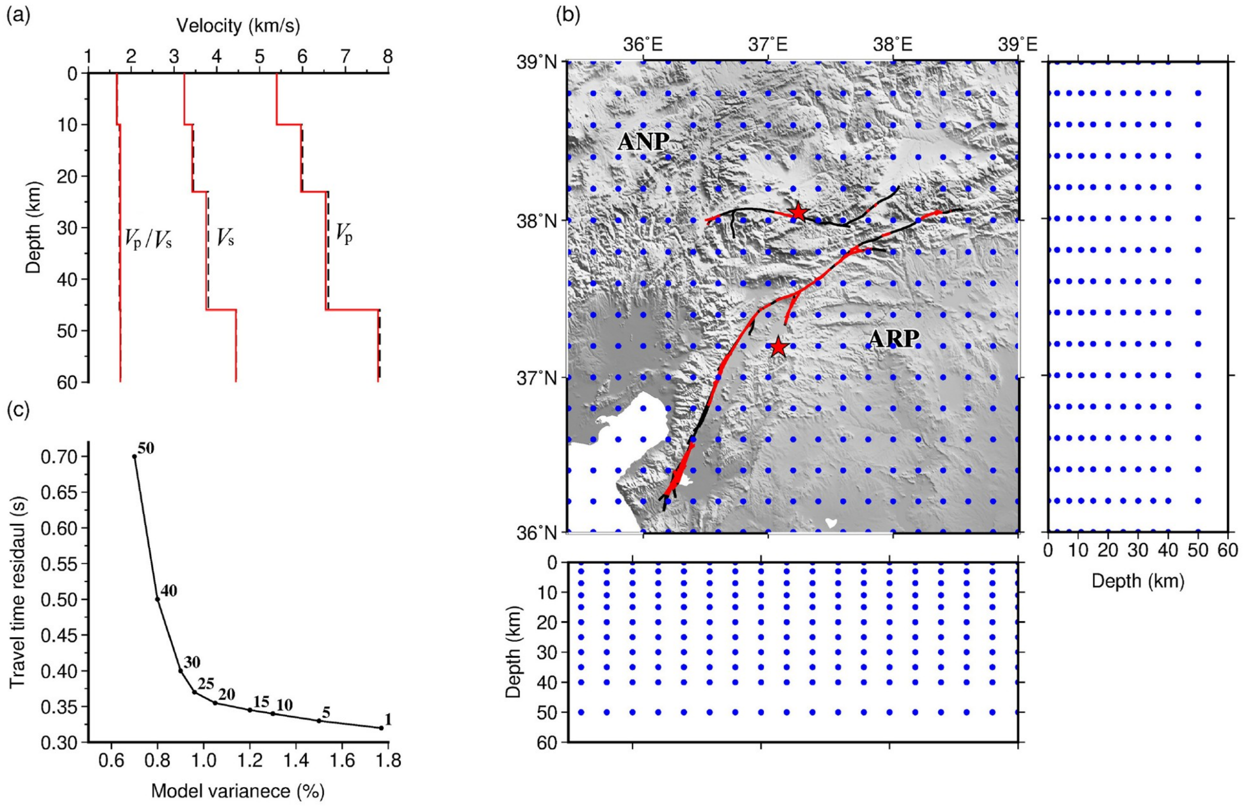

Figure 3 Initial parameterization for seismic tomographic inversion. (a) 1-D velocity models. The black dashed line represents the initial 1-D velocity model derived from previous seismic profiles (Medved et al., 2021), while the red solid line depicts the optimal velocity calculated from the final inverted seismic model in its 1-D version. (b) 3-D distribution of the grid model utilized in seismic tomography is depicted, with red and black solid lines representing the background fault and rupture sections, respectively. The blue dots indicate the grid nodes spaced at 0.2° horizontal intervals and have depth intervals ranging from 3 to 10 km. (c) The trade-off between travel time residuals and model variations using diverse damping parameters is shown. A damping value of 25 was chosen as the final parameter.

off curves between data fitness and model stability (Figure 3c). The resulting V_P, V_S, and V_P/V_S models are smoothed across grid nodes and visually represented after five iterations.

2.3 Hypocenter relocation and joint seismic tomography

In order to reduce the adverse impact of uncertainties in

Table 1 The seismic data utilized for the joint application of seismic tomography and hypocenter relocations

Type	Source-receiver pairs (P & S pairs; Pn & Sn pairs)		No. of events	No. of seismic stations	Recorded times (date/month/year)
Foreshocks	P & S pairs	23,905	3,812	238	01/03/2014-06/02/2023
	Pn &Sn pairs	11,249			
Aftershocks	P & S pairs	43,348	5,552	238	06/02/2023–30/03/2023
	Pn & Sn pairs	22,331			
Total	100,833		9,364	238	01/03/2014–27/03/2023

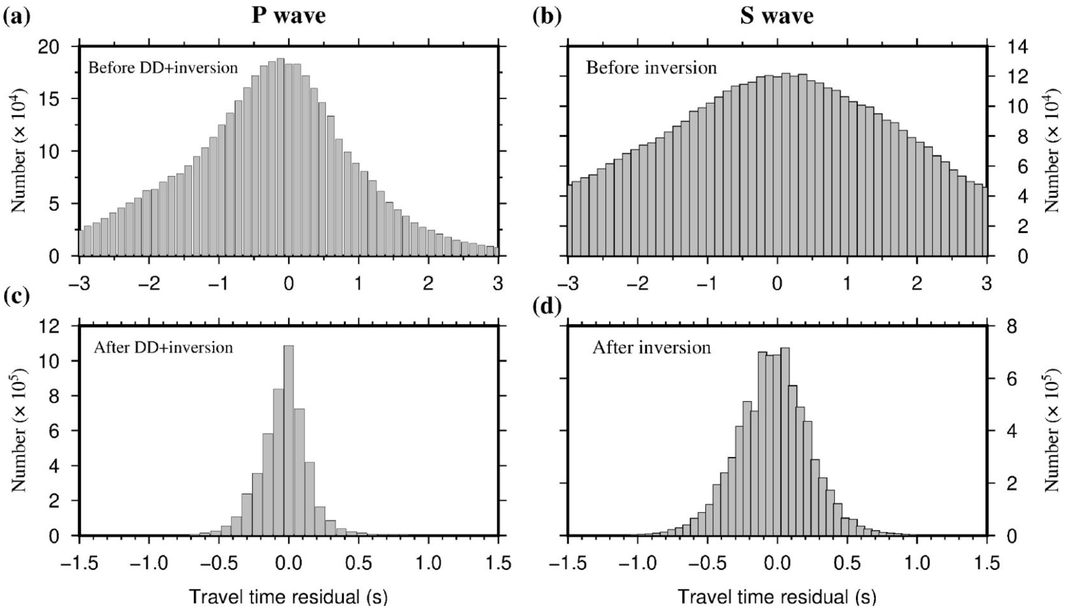

Figure 4 Histogram of P and S-wave travel time residuals, showing results before and after seismic tomographic inversions, where (a), (b) represent the former and (c), (d) depict the latter.

hypocenter locations on seismic tomography, we adopt a sequential approach to simultaneously determine high-resolution seismic velocities (V_P, V_S), Poisson's ratio (σ), and earthquake locations. Firstly, we employed the double-difference (DD) location technique to enhance the relocation accuracy of two clusters of earthquakes (Waldhauser and Ellsworth, 2000; Wang and Zhao, 2006). Subsequently, we performed seismic tomography analysis followed by iterative inversions of these two steps until satisfactory convergence was achieved. We selected 405,873 pairs of seismic events from a pool of 9364 local earthquakes. Utilizing these pairs, we relocated the relative hypocenters' locations using 1,980,216 double-difference travel times. Through three iterations with updated 3-D seismic structures simultaneously applied, our analysis successfully relocated over 95% (8943) of the total events. Figure 5 presents plain views and profiles illustrating the confined distribution of the majority of relocated aftershocks within prominent fault systems, including the EAF, the northernmost section of the DSF, and the Çardak Fault. After tomographic inversion, both P- and S-wave RMS of travel-time residuals exhibited a remarkable reduction by over 67% compared to their initial values (Figure 4).

Traditionally, tomographic images of V_P and V_S have been obtained separately from P- and S-wave travel-time residuals. The V_P/V_S ratio can be calculated from the independently inverted models of V_P and V_S, which can then be directly translated to Poisson's ratio σ (Eberhart-Phillips, 1986; Thurber, 1993). However, such indirectly derived σ may inherit a more significant error due to the combination of uncertainties in V_P and V_S. The parameter σ (or V_P/V_S ratio) is a physical property that exhibits sensitivity to lithology, temperature, degree of melting, and pore fluids (Hyndman, 1988; Sibson, 1992; Chevrot and van der Hilst, 2000). To ensure an unbiased σ model in this study, we implemented a tomographic scheme for simultaneous inversion of V_P and V_P/V_S using carefully selected source-receiver pairs based on P- and S-wave arrival times from a large dataset. The joint tomographic inversion approach employed in this study mostly follows the previous research conducted by Wang (2014) and others (Wang et al., 2019; Wang and Kao, 2019). Both P- and S-phase arrival times are essential for each

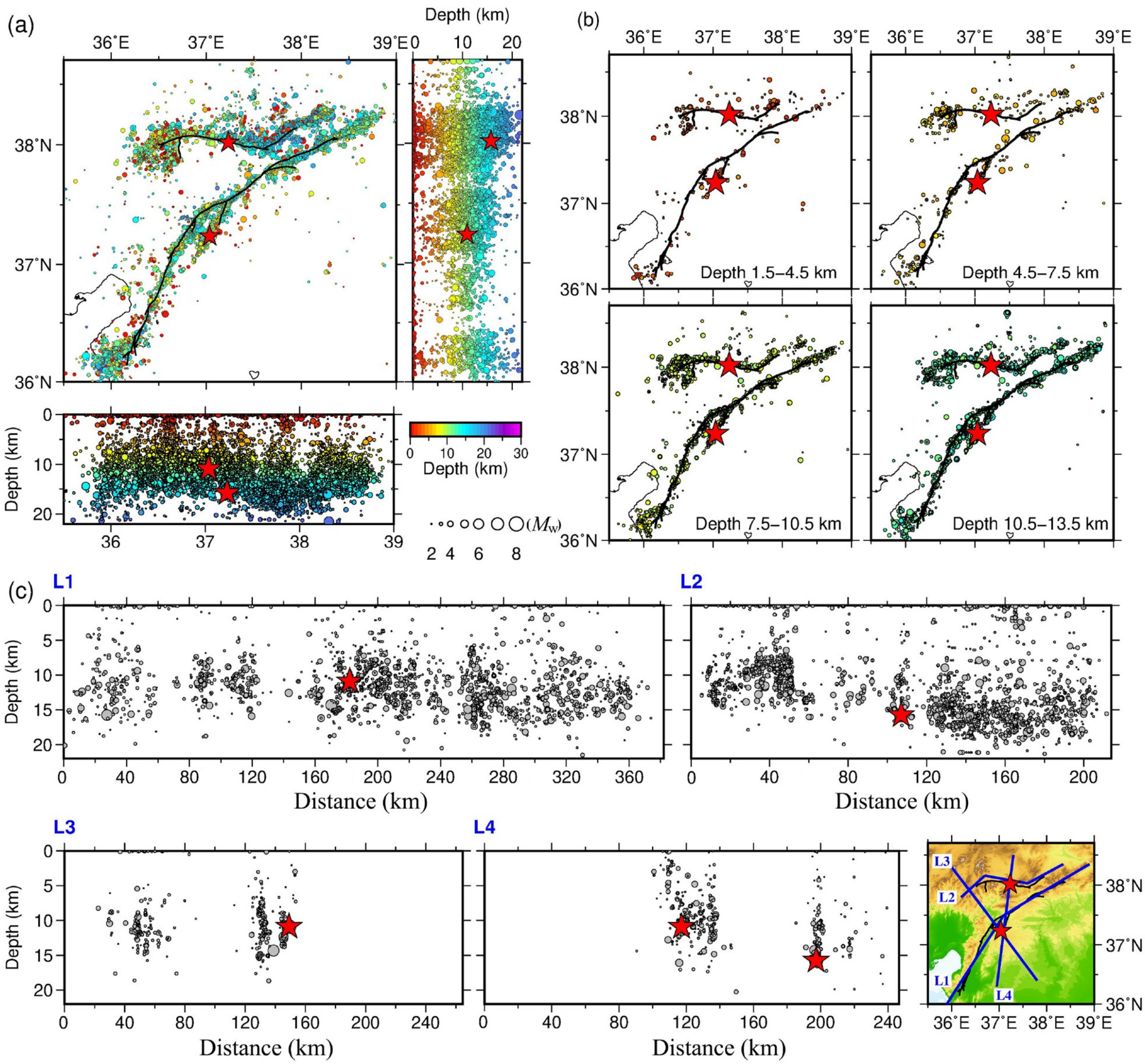

Figure 5 Distribution of aftershocks relocated using the DD relocation method. (a) 3D distribution of 9,364 earthquakes. Each circle represents one event, with size proportional to the magnitude and color dependent on depth; (b) map views of the relocated aftershock sequence at four different depth ranges; (c) vertical cross-sections of aftershocks across the dual hypocenters with a 5-km thickness bound to each profile. Red stars denote the mainshocks.

source-receiver pair to determine the corresponding V_P/V_S ratio. This approach directly constrains V_P/V_S by data exactly as it does for V_P, thereby avoiding any combined uncertainties associated with both parameters (Thurber, 1993; Wang, 2014; Wang et al., 2019; Wang and Kao, 2019). Once the joint tomography inversion of V_P and V_P/V_S is completed, the V_S structure is subsequently inverted solely using S-phase arrival times. In principle, due to distinct data constraints on each parameter, the V_S value obtained directly from S-wave arrival times may differ from that derived from the inverted values of V_P and V_P/V_S. However, the simultaneous utilization of P- and S-wave source-receiver pair data in determining V_P, V_S, and V_P/V_S values leads to concurrent determination. By employing the tomography inversion scheme developed by Wang et al. (2019) and Wang and Kao (2019), a high-resolution 3D V_P, V_S, and V_P/V_S structures within our study area are expected.

2.4 Synthetic tests for seismic tomography

As part of our seismic tomographic analysis, we conducted checkboard resolution tests (CRTs) to evaluate the appropriateness of parameter initialization for practical seismic tomography. We assigned velocity perturbations of ±3% to each adjacent grid node and computed synthetic travel-time data for the checkerboard model. Meanwhile, random errors with a standard deviation of 0.08 s for P-waves and 0.12 s for S-waves were incorporated into the synthetic data, considering their approximate uncertainties in actual travel-time data measurements.

The CRTs and subsequent actual tomography employed identical input parameters of events, stations, and ray paths. Based on the CRT results, we selected a horizontal grid spacing of 0.2° and a depth range between 3 km and 10 km of the initial grid model (Figure 6). This model configuration optimizes data resolution by considering the spatial distribution of sources and stations across the entire study area. The results of the CRT demonstrate a high resolution in delineating the rupture zones associated with the 2023 Türkiye earthquake doublet. Additionally, the spatial distribution of ray paths exhibits a dense crisscrossing that spans across the entire crust of the study region (Figure 2b, 2c), suggesting high resolution for capturing velocity perturbations using our input dataset. Therefore, we assert that the anomalies inferred from our tomography inversion exhibit well-resolved and dependable features (Figures 7 and 8).

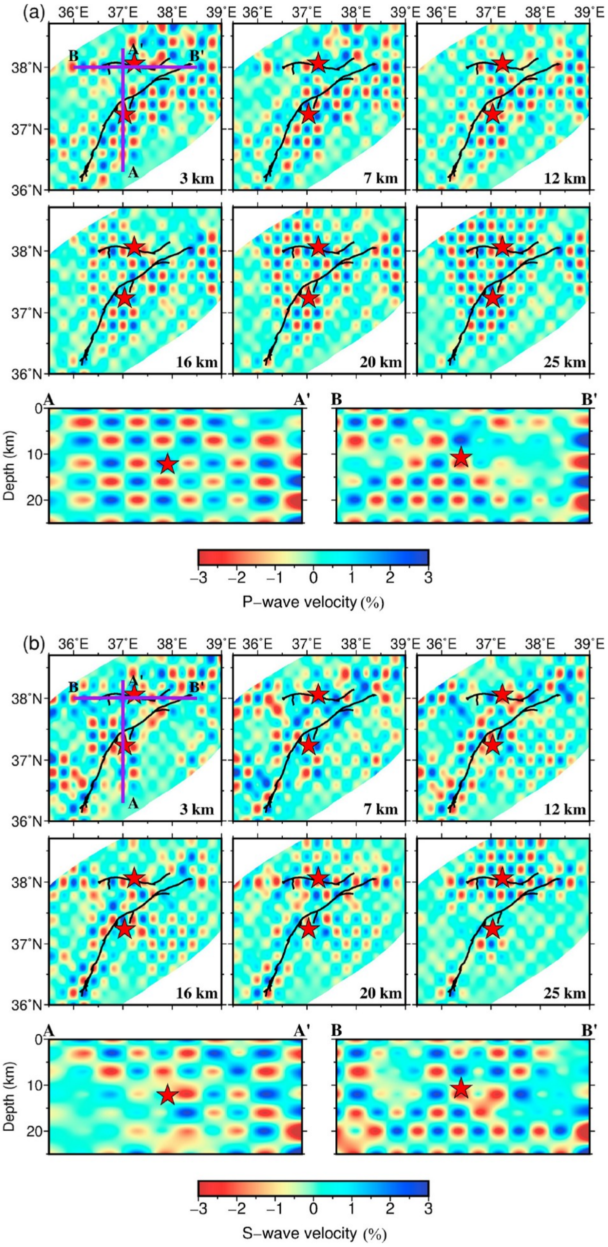

Figure 6 Map view and profiles of checkerboard resolution tests (CRTs) for (a) P- and (b) S-wave seismic tomography, respectively. A horizontal distance of 0.2° and depth intervals ranging from 3 to 10 km were used for the synthetic tests. The adjacent grid notes are alternately signed with ±3% perturbations of seismic velocities. Synthetic travel times were calculated from the same initial parameterized models, which were then used to invert the CRTs. The vertical cross-sections are located as indicated in the upper-left map, depicting P-wave CRTs and S-wave CRTs.

3. Results and interpretation

3.1 Aftershock distribution and seismic structural variations along rupture zones

The magnitudes of the earthquake doublet exceed expectations, likely due to the unexpected fault length scale and high-level crustal shear stress accumulations (Ambraseys and Jackson, 1998; Lin et al., 2021). The historical earthquake catalog reveals a wide range of magnitudes (ranging from M_w6+ to M_w7+) for earthquakes occurring in the rupture zones, leading to partial or complete strain release across various segments of the fault zone (Ambraseys and Jackson, 1998; Figure 1). This complex seismotectonic and faulting system may involve multiple fault segments in the 2023 earthquake doublet rupture processes. To better understand the cascade rupture growth during great earthquakes, we followed Yagi and Fukahata (2011) and analyzed the spatiotemporal distribution of early aftershocks and their correlations with the mainshock rupture processed along the dual rupture zones. Here, we defined the early aftershock sequences as the events occurring within 36 hours after the E1 event (Figure 1c). Based on the relocated aftershock sequences (Figure 5), a higher concentration of aftershocks is observed close to the two endpoints exhibiting significant surface displacement rather than in regions with the most pronounced displacement along the two rupturing zones (Figures 1b and 5). This observation can be attributed to a greater likelihood of local stress concentration occurring in the former, while stress release is more prominent in the latter. Additionally, the distribution of aftershocks subsequent to the M_w7.6 earthquake reveals deeper depths in the eastern section compared to those observed in the west/southwest sections, showing consistency with the high-velocity anomalies observed at various depths (refer to Figure 8b). These findings further revealed a strong correlation between early aftershock distributions and structural heterogeneities within the fault seismic zone (Figures 8 and 9).

Furthermore, the distribution of aftershocks (Figure 5c) reveals the presence of multiple clusters of seismicity associated with the E1 event, indicating a complex fault geometry and rupture process. The majority of aftershocks

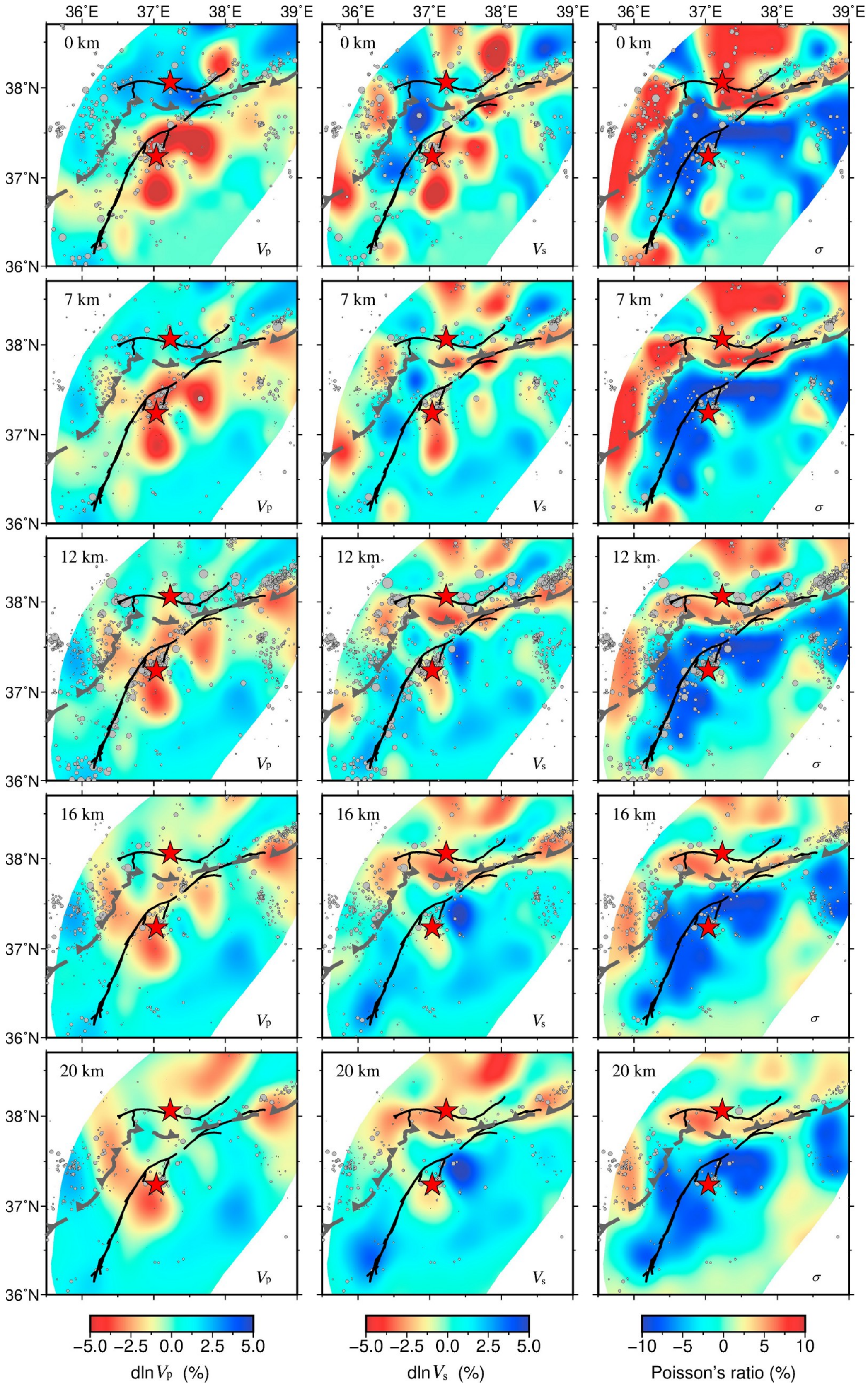

Figure 7 Map views of V_P, V_S, and Poisson's ratio (σ) (in percentage %) at five depths. The velocity anomalies are given with respect to the average velocity of each layer. Red stars represent two mainshocks. Black bold lines show the surface ruptures. Grey circles denote the aftershocks. The gray sawtooth lines mark the location of the SAT front.

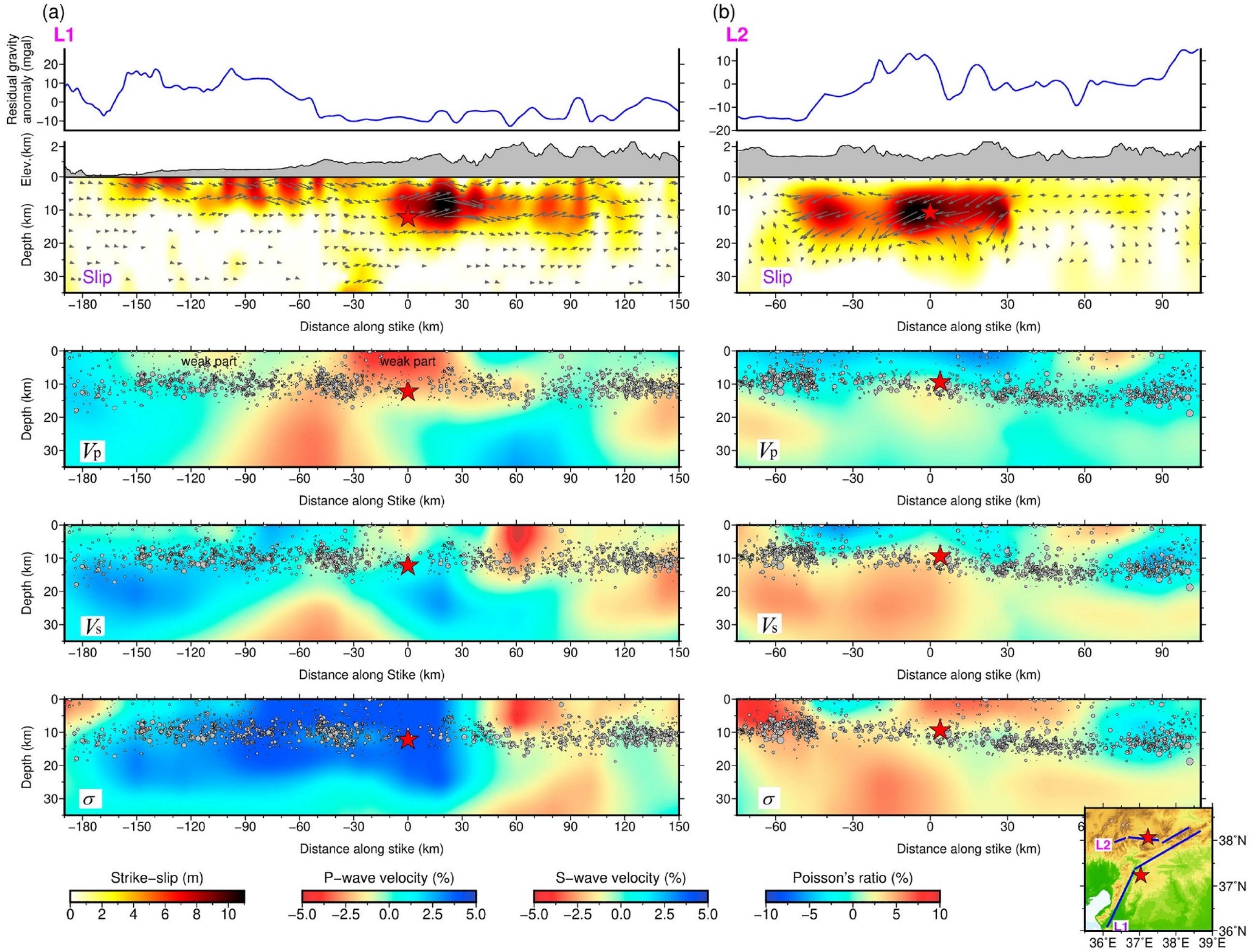

Figure 8 Distribution of seismic structures, residual gravity anomalies, and strike-slip characteristics along the dual rupture zones. (a) Vertical profiles along the EAF showing the crustal structure variations of the M_w7.8 earthquake. (b) Vertical cross-section along the Çardak Fault showing the crustal structure variations of the M_w7.6 earthquake. The gray dots on each profile indicate the relocated aftershocks with a thickness bound of approximately 10 km, while the red stars represent the hypocenters of the earthquake doublet. A blue solid line at the top of each profile indicates the residual gravity anomalies along the cross-section, calculated using Bouguer gravity data from Sandwell et al. (2014). The perturbation scales for V_P, V_S, and σ are shown at the bottom of the figure, while the inset map in the lower-right corner indicates the positions of the profiles.

(M_w>2.0) are concentrated in areas characterized by slightly higher V_S values and lower σ zones/edges, occurring at depths ranging from 5 km to 15 km along the E1 rupture zone (Figure 8). The spatiotemporal distribution of the initial nine-hour aftershocks indicates that all of them were confined within the DSF and EAF, excluding the Çardak Fault. However, the subsequent aftershocks can be observed along both previously identified faults as well as on the later ruptured Çardak Fault (Figure 1c). These findings indicate that the accumulated strain energy within the extensive slip zone was effectively released during the E1 rupture event (Figure 1c).

3.2 Strong structural anomalies along the dual rupture zones

Seismic structure heterogeneities within rupture zones are influenced by multiple factors, including geological settings, variations in rock properties, crustal stress variations, and fluid content (Hyndman, 1988; Sibson, 1992; Chevrot and van der Hilst, 2000; Wang et al., 2006; Wang and Zhao, 2006; Thurber et al., 2006; Pei et al., 2019; Wang et al., 2019; Wang and Kao, 2019; Sun et al., 2021). In the map view, distinct patterns of V_P and σ anomalies with sharp contrasts are clearly observed on either side of the SAT boundary (gray jagged line in Figures 1 and 10) (Legeay et al., 2019), reflecting contrasting tectonic frameworks. The observed seismic structural anomalies exhibit characteristics comparable to those observed along the San Andreas Fault in California (Thurber et al., 2006), as well as the 2021 M_w7.3 Maduo earthquake in Western China (Chen et al., 2022; Xiao et al., 2022; Ha et al., 2022). The presence of high-V_S and low-σ anomalies on the right-hand side indicates a northwestward movement of the Arabian platform, while the occurrence of a low-V_S and high-σ belt on the opposite side signifies thrust and fold nappe formation resulting from an arc-volcanic process associated with northward subduction of the Cyprus slab. If this hypothesis holds true, then both segments—the southwest segment within an Arabian domain and the northeast segment along the collision front—confine the E1 rupture zone. In contrast, the subsequent event is confined to a thrust domain characterized by low-V_S and high-σ anomalies (Figure 7). This suggests that although the EAF may not represent a tectonic boundary between plates, it is plausible that the SAT boundary could serve as one (Figures 1a and 7). These observations imply that the earthquake doublet occurred in distinct tectonic settings and different seismogenic environments, potentially contributing to their diverse rupture structures. Considering the high resolution demonstrated by the CRTs in the rupture zones of the 2023 Türkiye earthquake doublet, as well as the distribution of dense crisscrossing ray paths that cover the entire crust of the study area (Figure 2b, 2c), we consider these crustal seismic structures along these rupture zones as reliable features.

In the cross-section view, our seismic model has revealed significant structural variations in V_P, V_S, and σ along the 2023 doublet rupture zones (Figure 8). For instance, there is a lateral scale range of V_S values from high in the SW segment to low in the NE one along the E1 rupture zone. This variation is accompanied by corresponding changes in σ from low to high (Figure 8a), which are consistent with previous seismic and attenuation tomographic studies (e.g., Medved et al., 2021; Zhu et al., 2023). At shallow depths (~5 km) along the E1 rupture zone (Figure 8a), scattered regions exhibit relatively low-V, high-σ values, and reduced seismic activity. These areas display fewer surface displacements compared to other regions (Figure 9b), indicating weakened or ductile components. Although the V_P, V_S, and σ patterns exhibit similar features on a lateral scale, the E2 rupture zone displays a distinct contrast pattern of seismic parameters across different depths. High values of V and σ are observed within the upper 10 km, while contrasting parameters are found at greater depths (Figure 8b). Consequently, substantial disparities in seismic structure between these two rupture zones may potentially impact the rupturing processes of the doublet.

4. Discussion

4.1 Sharp contrast structures control the M_w7.8 intricated rupture process

Recent studies (e.g., Dal Zilio and Ampuero, 2023; Chen et al., 2023; Meng et al., 2024) have shown that the E1 rupture propagated bilaterally in the southwest (SW) and northeast (NE) directions along the EAFZ (Figure 9a). In the northernmost Sakçagöz-Narlı segment (~40 km length) of the DSF, characterized by a relatively brittle area with high-V_S and low-σ section, slight high-V_P anomalies were observed. This rupture originated from there and proceeded northeastward for approximately 140 km along the EAF within about 50 s before transitioning to the southwest segment. It extended ~130 km from its epicenter for about 30 s (Figure 8a). The bilateral rupture mode observed in this study bears a resemblance to the 1999 Izmit earthquake (M_w7.4) that occurred along the North Anatolian fault zone (Ozalaybey et al., 2002). The rupture process is primarily confined to the upper crust, spanning approximately 15 km in depth. The primary slip patch of the E1 event extends for about 280 km along a left-lateral strike-slip direction, exhibiting a peak slip of around 11 m. This spatial distribution coincides with aftershock activities (Figure 8a), as well as regions characterized by relatively high-V_S and low-σ anomalies (Figure 8a). Notably, the overall slip of the rupture observed in the NE segment surpasses that in SW (Figure 8a), owing to distinct seismic structural variations between these two sections and differences in localized plate tectonics.

From the perspective of regional tectonic settings, the northwestward collision front of the Arabian plate exhibits curvature, resulting in a higher accumulation of compression stress in the NE segment than in the SW segment. Moreover, within the NE segment, the SAT boundary intersects with surface rupture (Figures 1a and 8a), potentially leading to a complex and intense release of strain energy specifically in this region as opposed to the SW region. Conversely, along the entire E1 rupture zone at depths of rupture, there is an observed contrasting pattern of V_S and σ anomalies between the NE and SW segments but not for the V_P structure (Figure 8a). These characteristics likely reflect variations in rock properties such as mechanical strength, fault coupling (locked asperity), and decoupling (unlocked) occurring bi-directionally within the rupture zone (Figures 1 and 10a). The presence of these features can be utilized to interpret the observation that regions characterized by high energy release during rupture tend to exhibit a positive correlation with elevated seismic velocities (Thurber et al., 2006), whereas the cessation of rupture may be associated with relatively lower seismic velocities (Michael and Eberhart-Phillips, 1991; Pei et al., 2014). Consequently, due to the oblique collision system, coupling segments have the potential to accumulate higher crustal shear stress compared to decoupling parts (Pei et al., 2014, 2019; Sun et al., 2021; Wang et al., 2019). The onset of the E1 rupture is characterized by its high super-shear velocity (Ren et al., 2024), potentially extending through the locked fault section in the NE direction. Its cessation requires specific conditions at either end of the fault, such as strong rock mechanical strength (high-V and low-σ portions shown in Figure 10a). The presence of low-V_S and high-σ patches at depths shal-

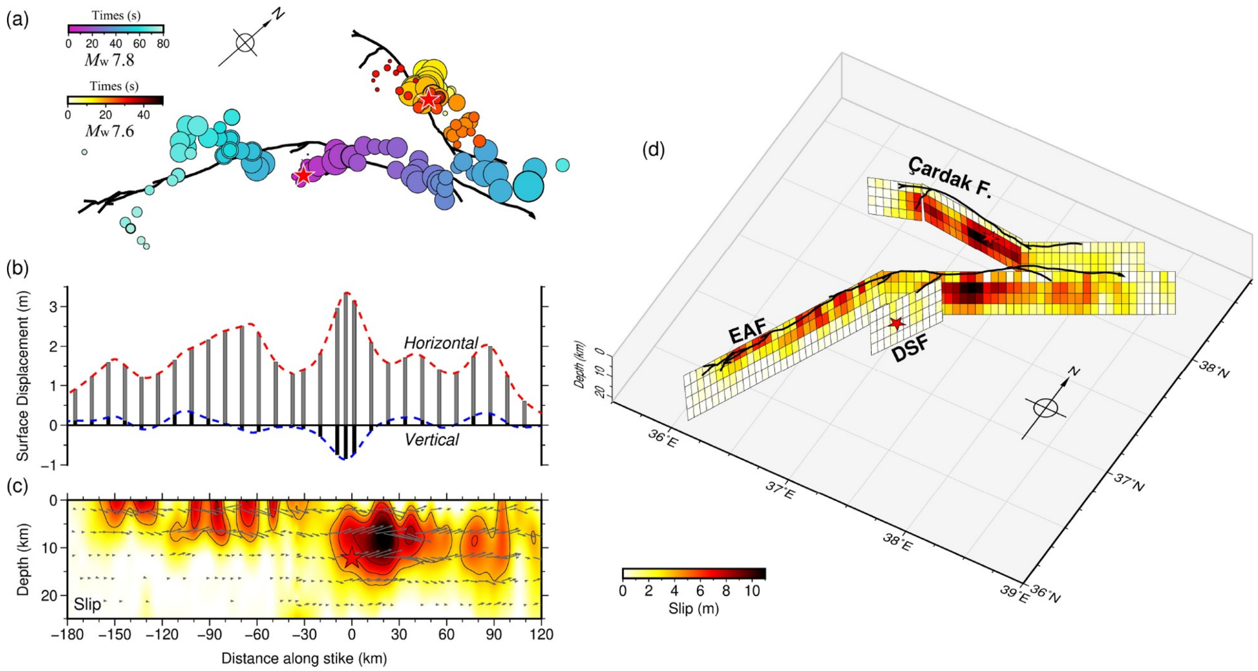

Figure 9 Illustrations of the distribution of space-time evolution and amplitudes of rupture, surface displacement, and coseismic slip along the rupturing zones of both mainshocks. (a) Space-time evolution and amplitudes of the back-projection results for the M_w7.8 and 7.6 Türkiye dual earthquakes, modified from a previous study (Chen et al., 2023). Different colors indicate distinct duration times of the aftershock migration. (b) Displays of the horizontal (red dash line) and vertical (blue dash line) surface displacement along the rupture zones of EAF, derived from the finite-fault modeling results (Goldberg et al., 2023). (c) Depicts of the strike-slip distribution of the first M_w7.8 earthquake. (d) 3-D visualization of coseismic slips along both rupture zones. SN DSF, Sakçagöz-Narlı segment of the Dead Sea Fault.

lower than 5 km suggests the existence of ductile regions with larger surface displacements (Figures 8a and 9b), indicating that the complex rupture process of E1 initiates in a relatively brittle section characterized by high crustal shear stress and easily propagates across bilateral weakened zones along the EAF (Figure 10a). Based on seismic structures and geological settings, we propose that changes in rock properties within the upper crust associated with the southeast Anatolian thrust and fold zone juxtaposed with the comparatively robust Arabian continental crust primarily contribute to the complex rupture process of the E1 event (Figure 10a).

4.2 Role of fluids in the M_w7.6 rupture process

Although the E2 rupture also propagated bilaterally, the concurrent ruptures in both east and west directions distinguish it from the E1 cascade rupture (Figures 8b and 9a). The initiation of the E2 rupture occurred within a region characterized by low-V and high-σ anomalies, followed by a westward propagation over a distance of approximately 60 km within a time frame of roughly 20 s. Simultaneously, it extended eastward for about 50 km during the course of around 30 s (Figures 8b and 9a). The primary slip patch associated with the E2 event covered an area of approximately 110 km along the strike within the uppermost ~16 km crustal layer. This value aligns with the focal depth distribution of aftershocks (Figure 8b). The aftershocks occurring on the eastern side are situated at a greater depth compared to those on the western side along the rupture zone, which can be attributed to variations in rock properties between these two segments as evidenced by significant changes in V_P, V_S, and σ parameters (Figure 8b). Comparable seismic velocity patterns are observed in both directions along the E2 fault zone, albeit with varying anomalous amplitudes (Figure 8b). The observed patterns align with regions of high attenuation (low Lg-wave value) in the eastern margin of the Anatolian plateau, particularly for our σ images, as documented by Zhu et al. (2023). A majority of aftershocks from E2 earthquakes occur at depths where there are anomalies characterized by low-to-high V_P, low-V_S, and high-σ values (Figure 8b). This implies that the mechanical strength of the rock in these areas has been comparatively weakened compared to a typical seismogenic zone. Additionally, it was observed that the left-lateral strike-slip activity of the E2 rupture in the western part of the rupture zone exhibited greater magnitudes compared to its eastern counterpart. This observation is consistent with high-V and low-σ anomalies detected in crustal structures within a depth range of 10 km (Figure 8b). Moreover, a distinct body characterized by low-V and high-σ values is clearly evident beneath the initial rupture zone of E2, where peak slip values reach approximately 11 m (Figure 8b), indicating a potential presence of fluids within the crust. The anomalous body with

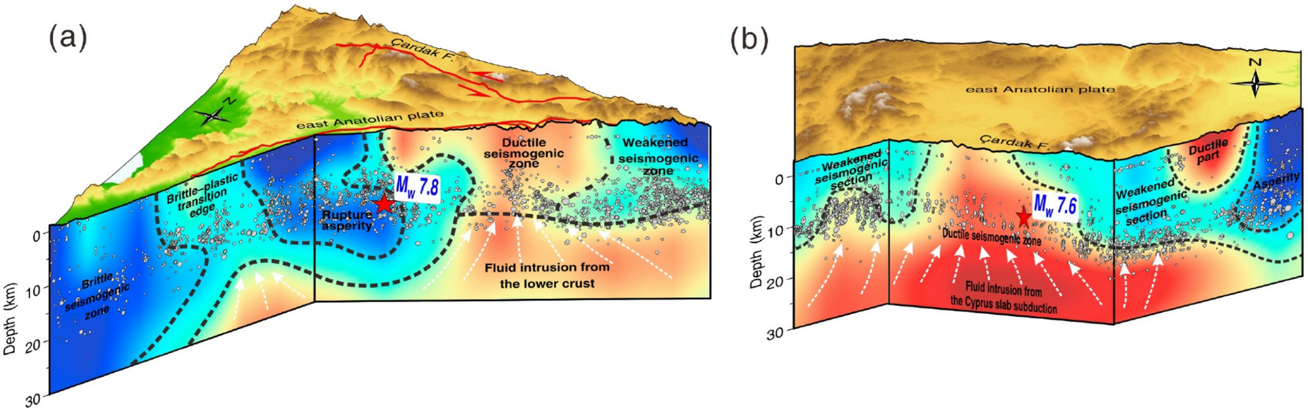

Figure 10 Schematic models of the structural heterogeneity and rupture processes for the M_w7.8 earthquake rupturing primarily along the EAF (a), and the M_w7.6 earthquake rupturing along the Çardak Fault (b). The hypocenters of both mainshocks are denoted by two red stars. The dark blue color represents a strong fault coupling (asperity) characterized by a brittle and dry seismogenic zone, while the red color indicates a ductile/plastic seismogenic zone with weak fault coupling (decoupling) (Pei et al., 2010, 2014, 2019; Wang et al., 2015, 2021). White arrows indicate the direction of possible fluid migration. Grey circles show the aftershocks.

low V_S and high σ is commonly associated with fluid occurrences due to their sensitivities towards fluids. It should be noted that the northward subduction of the Cyprus slab and its subsequent detachment may result in significant fluid release from deep depths.

Moreover, the thickened Anatolian plateau increases crustal pressure and temperature in the lower crust, leading to partial melting as supported by numerous previous studies (e.g., Türkoğlu et al., 2008; Hacıoğlu et al., 2018; Zhu et al., 2023). Consequently, fluids released from slab dehydration can infiltrate into the weakened or fractured seismogenic zone through cracks with high porosities, inducing a decrease in rock mechanical strength, reducing static stress threshold value, and elevating fluid pore pressure within the E2 rupture zone. The distinct seismic structures may have further influenced the rupture mechanism of E2 (Figure 10b), which differs from the observed rupturing process in E1 (Figure 10a). Meanwhile, it is possible that the occurrence of the E1 earthquake has attenuated shear stress on the E2 fault, thereby impeding the immediate initiation of an E2 rupture. However, this event may have concurrently and significantly reduced the normal stress exerted on the E2 fault owing to a double left-lateral strike-slip system within a triangular region (Figure 1a). The normal stress reduction not only contributes to a decrease in fault friction force and an increase in rock porosity, thereby facilitating fluid intrusion into the opened cracks, but also leads to lower strain drops and the redistribution of Coulomb stress and dynamic strains (Ozalaybey et al., 2002; Yang et al., 2009; Liu et al., 2023; Jia et al., 2023). This plausibly promotes the initiation of the E2 event in a ductile zone, providing a reasonable explanation for why the E2 rupture occurred nine hours after the E1 event. The time required for fluid infiltration into the E2 source region from deep depths through cracks or faults could have played a crucial role in this delay.

5. Conclusions

Our high-resolution 3-D seismic structures have revealed that the initiation of the M_w7.8 rupture occurred within a brittle segment characterized by high-V_S and low-σ anomalies within the seismogenic zone along the EAF, while the M_w7.6 rupture originated in a ductile belt featuring low-V_P, low-V_S, and high-σ values expanding along the Çardak Fault. Relocated aftershocks indicate that multiple faults were involved in both rupturing processes; however, the former process exhibits greater complexity compared to the latter. The pronounced heterogeneities observed in crustal seismic structures, manifesting as sharp variations in rock physical properties, have played a pivotal role in these dual diverse rupturing processes. These variations in seismic parameters are primarily attributed to the localized geological settings associated with either the oblique colliding system between the Anatolian plateau and Arabian plate or the northward subduction of the Cyprus slab followed by subsequent delamination. The M_w7.8 rupture is characterized by brittle crustal deformation, with distinct rupture processes in the NE and SW segments of the rupture zone.

On the other hand, the M_w7.6 earthquake is attributed to ductile fault failure resulting from fluid intrusion into a weakened seismogenic zone driven by high fluid-pore pressure. Furthermore, the occurrence of the initial earthquake may influence subsequent events by concurrently reducing both shear stress and normal stress on the Çardak Fault, thereby decreasing fault friction force and increasing rock porosity, which contributes to the initiation of the second event. Our study not only provides new insights into the rupture processes of the earthquake doublet but also offers crucial information for mitigating earthquake disasters in Türkiye or Europe.

Acknowledgements *We would like to express our sincere gratitude to the responsible editor and anonymous reviewers for their invaluable feedback that has significantly enhanced the quality of this paper. Special thanks are extended to Dr. Dun WANG for providing the earthquake rupture front propagation data and Rita Kounoudis for sharing the Cyprus slab data. The surface displacement data utilized in this study were obtained from the U.S. Geological Survey (USGS), https://earthquake.usgs.gov/earthquakes/. All arrival time data used in this study were acquired from the Disaster and Emergency Management Authority (AFAD), https://deprem.afad.gov.tr/event-catalog. Figures were generated using the Generic Mapping Tool. Access to the final 3D seismic models is available through the Open database at https://doi.org/10.5281/zenodo.8189093. This study was funded by the National Natural Science Foundation of China (Grant Nos. 42241206, 92058210, 42074047, U2039203, 42130306).*

Conflict of interest The authors declare that they have no conflict of interest.

References

Ambraseys N N, Jackson J A. 1998. Faulting associated with historical and recent earthquakes in the eastern Mediterranean Region. Geophys J Int, 133: 390–406

Barbot S, Luo H, Wang T, Hamiel Y, Piatibratova O, Javed M T, Braitenberg C, Gurbuz G. 2023. Slip distribution of the February 6, 2023 M_w7.8 and M_w7.6, Kahramanmaraş, Turkey earthquake sequence in the East Anatolian Fault Zone. Seismica, 2: 502

Chen W, Wang D, Can Z, Qiang Y, Si H. 2022. Estimating seismic intensity maps of the 2021 M_w7.3 Madoi, Qinghai and M_w 6.1 Yangbi, Yunnan, China Earthquakes. J Earth Sci, 33: 839–846

Chen W, Rao G, Kang D, Wan Z, Wang D. 2023. Early report of the source characteristics, ground motions, and casualty estimates of the 2023 M_w7.8 and 7.5 Turkey Earthquakes. J Earth Sci, 34: 297–303

Chevrot S, van der Hilst R D. 2000. The Poisson ratio of the Australian crust: Geological and geophysical implications. Earth Planet Sci Lett, 183: 121–132

Dal Zilio L, Ampuero J P. 2023. Earthquake doublet in Turkey and Syria. Commun Earth Environ, 4: 71

Duman T Y, Emre Ö. 2013. The East Anatolian Fault: Geometry, segmentation and jog characteristics. Geol Soc Lond Spec Publ, 372: 495–529

Eberhart-Phillips D. 1986. Three-dimensional velocity structure in northern California coast ranges from inversion of local earthquake arrival times. Bull Seismol Soc Amer, 76: 1025–1052

Emre Ö, Duman T Y, Özalp S, Şaroğlu F, Olgun Ş, Elmacı H, Çan T. 2018. Active fault database of Turkey. Bull Earthquake Eng, 16: 3229–3275

Goldberg D E, Taymaz T, Reitman N G, Hatem A E, Yolsal-Çevikbilen S, Barnhart W D, Irmak T S, Wald D J, Öcalan T, Yeck W L, Özkan B, Jobe J A T, Shelly D R, Thompson E M, DuRoss C B, Earle P S, Briggs R W, Benz H, Erman C, Doğan A H, Altuntaş C. 2023. Rapid characterization of the February 2023 Kahramanmaraş, Türkiye, earthquake sequence. Seismic Rec, 3: 156–167

Gülerce Z, Tanvir Shah S, Menekşe A ı, Arda Özacar A, Kaymakci N, Önder Çetin K. 2017. Probabilistic seismic-hazard assessment for East Anatolian Fault Zone using planar fault source models. Bull Seismol Soc Am, 107: 2353–2366

Ha G, Liu J, Ren Z, Zhu X, Bao G, Wu D, Zhang Z. 2022. The interpretation of seismogenic fault of the Maduo M_w7.3 Earthquake, Qinghai based on remote sensing images—A branch of the east Kunlun fault system. J Earth Sci, 33: 857–868

Hacıoğlu Ö, Başokur A T, Çiftçi E T. 2018. Crustal structure of a young collision zone: The Arabia-Eurasia collision in northeastern Turkey investigated by magnetotelluric data. Earth Planets Space, 70: 161

Hall S. 2023. What Turkey's earthquake tells us about the science of seismic forecasting. Nature, 615: 388–389

Hussain E, Kalaycıoğlu S, Milliner C W D, Çakir Z. 2023. Preconditioning the 2023 Kahramanmaraş (Türkiye) earthquake disaster. Nat Rev Earth Environ, 4: 287–289

Hyndman R D. 1988. Dipping seismic reflectors, electrically conductive zones, and trapped water in the crust over a subducting plate. J Geophys Res, 93: 13391–13405

Jia Z, Jin Z, Marchandon M, Ulrich T, Gabriel A A, Fan W, Shearer P, Zou X, Rekoske J, Bulut F, Garagon A, Fialko Y. 2023. The complex dynamics of the 2023 Kahramanmaraş, Turkey, M_w7.8-7.7 earthquake doublet. Science, 381: 985–990

Kagan Y Y, Jackson D D. 1999. Worldwide doublets of large shallow earthquakes. Bull Seismological Soc Am, 89: 1147–1155

Kahle H G, Cocard M, Peter Y, Geiger A, Reilinger R, Barka A, Veis G. 2000. GPS-derived strain rate field within the boundary zones of the Eurasian, African, and Arabian Plates. J Geophys Res, 105: 23353–23370

Kaviani A, Paul A, Moradi A, Mai P M, Pilia S, Boschi L, Rümpker G, Lu Y, Tang Z, Sandvol E. 2020. Crustal and uppermost mantle shear wave velocity structure beneath the Middle East from surface wave tomography. Geophys J Int, 221: 1349–1365

Kounoudis R, Bastow I D, Ogden C S, Goes S, Jenkins J, Grant B, Braham C. 2020. Seismic tomographic imaging of the Eastern Mediterranean mantle: Implications for terminal-stage subduction, the uplift of Anatolia, and the development of the North Anatolian Fault. Geochem Geophys Geosyst, 21: e2020GC009009

Legeay E, Pichat A, Kergaravat C, Ribes C, Callot J P, Ringenbach J C, Bonnel C, Hoareau G, Poisson A, Mohn G, Crumeyrolle P, Kavak K S, Temiz H. 2019. Geology of the Central Sivas Basin (Turkey). J Maps, 15: 406–417

Lin X, Hao J, Wang D, Chu R, Zeng X, Xie J, Zhang B, Bai Q. 2021. Coseismic slip distribution of the 24 January 2020 M_w6.7 Doganyol earthquake and in relation to the foreshock and aftershock activities. Seismol Res Lett, 92: 127–139

Liu C, Lay T, Wang R, Taymaz T, Xie Z, Xiong X, Irmak T S, Kahraman M, Erman C. 2023. Complex multi-fault rupture and triggering during the 2023 earthquake doublet in southeastern Türkiye. Nat Commun, 14: 5564

Medved I, Polat G, Koulakov I. 2021. Crustal structure of the eastern Anatolia Region (Turkey) based on seismic tomography. Geosciences, 11: 91

Melgar D, Taymaz T, Ganas A, Crowell B, Öcalan T, Kahraman M, Tsironi V, Yolsal-Çevikbil S, Valkaniotis S, Irmak T S, Eken T, Erman C, Özkan B, Dogan A H, Altuntaş C. 2023. Sub- and super-shear ruptures during the 2023 M_w7.8 and M_w7.6 earthquake doublet in SE Türkiye. Seismica, 2: 387

Meng J, Kusky T, Mooney W D, Bozkurt E, Bodur M N, Wang L. 2024. Surface deformations of the 6 February 2023 earthquake sequence, eastern Türkiye. Science, 383: 298–305

Michael A J, Eberhart-Phillips D. 1991. Relations among fault behavior, subsurface geology, and three-dimensional velocity models. Science, 253: 651–654

Ozalaybey S, Ergin M, Aktar M, Tapırdamaz C, Bicmen F, Yörük A. 2002. The 1999 Izmit Earthquake sequence in Turkey: Seismological and tectonic aspects. Bull Seismol Soc Am, 92: 376–386

Pasyanos M E, Masters T G, Laske G, Ma Z. 2014. LITHO1.0: An updated crust and lithospheric model of the Earth. J Geophys Res-Solid Earth, 119: 2153–2173

Pei S P, Su J, Zhang H, Sun Y, Toksöz M N, Wang Z, Gao X, Liu-Zeng J, He J. 2010. Three-dimensional seismic velocity structure across the 2008 Wenchuan M_s8.0 earthquake, Sichuan, China. Tectonophysics, 491: 211–217

Pei S P, Zhang H, Su J, Cui Z. 2014. Ductile gap between the Wenchuan and Lushan Earthquakes revealed from the two-dimensional Pg seismic tomography. Sci Rep, 4: 6489

Pei S P, Niu F, Ben-Zion Y, Sun Q, Liu Y, Xue X, Su J, Shao Z. 2019. Seismic velocity reduction and accelerated recovery due to earthquakes on the Longmenshan fault. Nat Geosci, 12: 387–392

Ren C, Wang Z, Taymaz T, Hu N, Luo H, Zhao Z, Yue H, Song X D, Shen

Z K, Xu H, Geng J H, Zhang W, Wang T, Ge Z, Irmak T S, Erman C, Zhou Y, Li Z, Xu H, Cao B, Ding H. 2024. Supershear triggering and cascading fault ruptures of the 2023 Kahramanmaraş, Türkiye, earthquake doublet. Science, 383: 305–311

Sandwell D T, Müller R D, Smith W H F, Garcia E, Francis R. 2014. New global marine gravity model from CryoSat-2 and Jason-1 reveals buried tectonic structure. Science, 346: 65–67

Sibson R H. 1992. Implications of fault-valve behaviour for rupture nucleation and recurrence. Tectonophysics, 211: 283–293

Sun Q, Pei S P, Cui Z X, Chen Y J, Liu Y B, Xue X T, Li J W, Li L, Zuo H. 2021. Structure-controlled asperities of the 1920 Haiyuan M8.5 and 1927 Gulang M8 earthquakes, NE Tibet, China, revealed by high-resolution seismic tomography. Sci Rep, 11: 5090

Thurber C H. 1993. Local earthquake tomography velocity and V_P/V_S theory. In: Iyer H M, Hirahara K, eds. Seismic Tomography: Theory and Practice. London: Chapman & Hall. 563–580

Thurber C H, Zhang H, Waldhauser F, Hardebeck J, Michael A, Eberhart-Phillips D. 2006. Three-dimensional compressional wavespeed model, earthquake relocations, and focal mechanisms for the Parkfield, California, Region. Bull Seismol Soc Am, 96: S38–S49

Turkelli N, Sandvol E, Zor E, Gok R, Bekler T, Al-Lazki A, Karabulut H, Kuleli S, Eken T, Gurbuz C, Bayraktutan S, Seber D, Barazangi M. 2003. Seismogenic zones in eastern Turkey. Geophys Res Lett, 30: 8039

Türkoğlu E, Unsworth M, Çağlar İ, Tuncer V, Avşar Ü. 2008. Lithospheric structure of the Arabia-Eurasia collision zone in eastern Anatolia: Magnetotelluric evidence for widespread weakening by fluids. Geology, 36: 619–622

USGS. US Geological Survey. 2023. Event page of 2023 M_w7.8 and M_w7.5 Kahramanmaraş Earthquake Sequence. https://earthquake.usgs.gov/earthquakes/eventpage/us6000jllz/finite-fault

Waldhauser F, Ellsworth W. 2000. A double-difference earthquake location algorithm: Method and application to the northern Hayward Fault, California. Bull Seismol Soc Am, 90: 1353–1368

Wang Z, Zhao D. 2006. Seismic images of the source area of the 2004 Mid-Niigata prefecture earthquake in Northeast Japan. Earth Planet Sci Lett, 244: 16–31

Wang Z, Kao H. 2019. The significance of tomographic edge zones for large earthquakes in Taiwan. J Geophys Res-Solid Earth, 124: 11822–11839

Wang Z. 2014. Joint inversion of P-wave velocity and V_P/V_S ratio and its application for imaging the deep structure in Northeastern Japan. Appl Geophys, 11: 119–127

Wang Z, Zhao D, Mishra O P, Yamada A. 2006. Structural heterogeneity and its implications for the low frequency tremors in Southwest Japan. Earth Planet Sci Lett, 251: 66–78

Wang Z, Su J, Liu C, Cai X. 2015. New insights into the generation of the 2013 Lushan Earthquake (M_s7.0), China. J Geophys Res-Solid Earth, 120: 3507–3526

Wang Z, Fukao Y, Miyakawa A, Hasegawa A, Takei Y. 2019. Crustal extension and graben formation by fault slip-associated pore opening, Kyushu, Japan. J Geophys Res-Solid Earth, 124: 4879–4894

Wang Z, Wang J, Yang X. 2021. The role of fluids in the 2008 M_s8.0 Wenchuan earthquake, China. J Geophys Res-Solid Earth, 126: e2020JB019959

Xiao L, Zheng R, Zou R. 2022. Coseismic slip distribution of the 2021 M_w7.4 Maduo, Qinghai Earthquake estimated from InSAR and GPS measurements. J Earth Sci, 33: 885–891

Yagi Y, Fukahata Y. 2011. Rupture process of the 2011 Tohoku-oki earthquake and absolute elastic strain release. Geophys Res Lett, 38: L19307

Yang W, Peng Z, Ben-Zion Y. 2009. Variations of strain-drops of aftershocks of the 1999 İzmit and Düzce earthquakes around the Karadere-Düzce branch of the North Anatolian Fault. Geophys J Int, 177: 235–246

Zhu W M, Zhao L F, Xie X B, He X, Zhang L, Yao Z X. 2023. High-resolution broadband Lg attenuation structure of the Anatolian crust and its implications for mantle upwelling and plateau uplift. Geophys Res Lett, 50: e2023GL103470

(Editorial handling: Zhigang PENG)